Pergamon

Geochimica et Cosmochimica Acta, Vol. 66, No. 22, pp. 3943–3954, 2002

0016-7037/02 $22.00 + .00

PII S0016-7037(00)00971-7

X-ray absorption spectroscopy study of Cu^{2+} and Zn^{2+} adsorption complexes at the calcite surface: Implications for site-specific metal incorporation preferences during calcite crystal growth

E. J. ELZINGA* and R. J. REEDER

Department of Geosciences, State University of New York, Stony Brook, NY 11794-2100, USA

(*Received October* 5, 2001; *accepted in revised form May* 6, 2002)

Abstract—We report results from in situ extended X-ray absorption fine structure (EXAFS) spectroscopy studies of Cu(II) and Zn(II) complexes forming at the calcite surface following adsorption from preequilibrated calcite-saturated solutions. Both Cu(II) and Zn(II) coordinate at Ca sites on the calcite surface, forming mononuclear inner-sphere adsorption complexes. The Zn adsorption complexes are in tetrahedral coordination with first-shell O neighbors with $R_{Zn\text{-}O}$ = 1.95 Å, and the Cu complexes are Jahn-Teller distorted, with equatorial $R_{Cu\text{-}O}$ = 1.95 Å. Results from EXAFS data of dilute Cu- and Zn-calcite solid solutions confirm substitution of these metals in the Ca site of the calcite structure as octahedral complexes during coprecipitation. X-ray fluorescence microanalyses of calcite ($10\bar{1}4$) hillocks grown in coprecipitation experiments show that divalent Cu and Zn, which have ionic radii smaller than Ca, are preferentially incorporated into the parallel arrays of $<\bar{4}41>_+$ steps that define one pair of symmetrically equivalent vicinal faces on polygonized growth spirals. In contrast, other divalent metals with sixfold ionic radii smaller than Ca (Co, Cd, Mn, Mg) have been shown to be preferentially incorporated into $<\bar{4}41>_-$ growth steps, which define the second pair of vicinal faces on the growth spirals, but which are symmetrically nonequivalent to the steps on the first pair. The distortion from octahedral symmetry observed for the Cu and Zn adsorption complexes likely plays a key role in the observed preference of Cu and Zn for incorporation into the $<\bar{4}41>_+$ steps. *Copyright © 2002 Elsevier Science Ltd*

1. INTRODUCTION

The incorporation of trace metals into calcite has been a major focus of investigators in a wide variety of disciplines. Trace element abundances and their distributions in carbonates are used as tracers of petrogenetic and diagenetic histories, as proxies for changes in ocean chemistry and paleoclimate, as sinks in geochemical cycles, and more recently, for predicting the effectiveness of sequestration of contaminants. Because of the importance of carbonates in so many near-surface environments, the factors controlling metal incorporation have been studied in considerable detail. Mucci and Morse (1990) and Rimstidt et al. (1998) provide excellent reviews of previous work examining experimental determinations of partition coefficients at or near room temperature. A principal conclusion of these studies is that experimentally determined partition coefficients for metal coprecipitation with calcite are invariably nonequilibrium, being controlled by kinetic and mechanistic factors specific to the experimental methods. Nonequilibrium partitioning is demonstrated by the growth rate effect, where experimentally determined partition coefficients of divalent cations vary systematically with the calcite growth rate (e.g., Lorens, 1981; Morse and Bender, 1990).

Other factors may also cause experimentally determined partition coefficients to deviate from equilibrium values. Among these additional factors, the influence of the mineral surface and related surface processes are the least explored. An example of how surfaces may influence metal incorporation is found in sector zoning, where metal incorporation differs between symmetrically nonequivalent faces of a calcite crystal. The origin of such surface influences on element incorporation is better seen on individual growth faces, particularly the common ($10\bar{1}4$) face of calcite, which typically grows by the spiral mechanism. Paquette and Reeder (1990) showed that growth steps on the ($10\bar{1}4$) face are predominantly parallel to the symmetrically equivalent [$\bar{4}41$] and [$48\bar{1}$] periodic bond chains (PBCs), which define the edges of the common cleavage rhombohedron. Growth steps spreading in opposite directions but parallel to the same PBC are symmetrically nonequivalent and usually distinguished with "+" and "−" subscripts. Polygonized growth spirals typically exhibit four flanks (vicinal faces), which are composed of arrays of growth steps parallel to one of these PBCs and with a unique direction of spreading. Examples are shown in Figure 1. The dynamic operation of these growth spirals, including the kinetic anisotropy between the nonequivalent steps, has been elegantly documented by in situ atomic force microscopy (Gratz et al., 1993; Teng et al., 1999; Davis et al., 2000). Paquette and Reeder (1995) and Reeder (1996) showed that divalent metals larger than Ca (e.g., Sr and Ba) are enriched in the $[\bar{4}41]_+$ and $[48\bar{1}]_+$ steps, (collectively denoted by $<\bar{4}41>_+$), whereas Mg, Co, Mn, and Cd, which are smaller than Ca, are preferentially incorporated in the $[\bar{4}41]_-$ and $[48\bar{1}]_-$ steps (denoted by $<\bar{4}41>_-$). This selectivity for different growth steps demonstrates that structural aspects of growth steps (or the incorporation sites within them) influence the incorporation process. Moreover, the different preferences exhibited for the larger and smaller cations suggest stereochemical aspects of the incorporation sites are sensitive to ion size.

* Author to whom correspondence should be addressed (eelzinga@notes.cc.sunysb.edu).

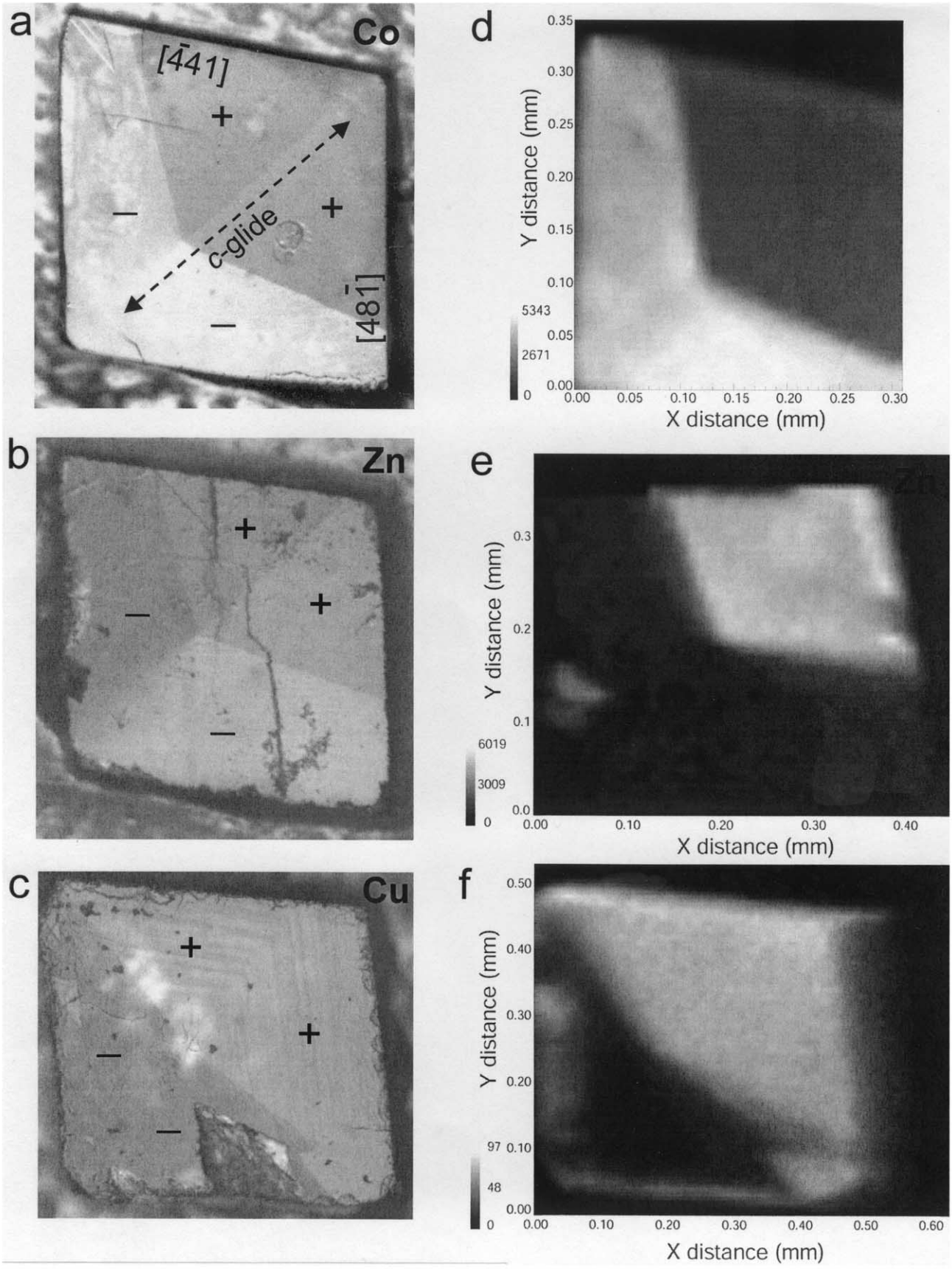
a
Co
[4̄41]
+
−
c-glide
+
−
[48̄1]
b
Zn
+
−
+
−
c
Cu
+
+
−
−
d
Y distance (mm)
0.35
0.30
0.25
0.20
0.15
0.10
0.05
0.00
5343
2671
0
0.00 0.05 0.10 0.15 0.20 0.25 0.30
X distance (mm)
e
Y distance (mm)
0.3
0.2
0.1
0.0
6019
3009
0
0.00 0.10 0.20 0.30 0.40
X distance (mm)
f
Y distance (mm)
0.50
0.40
0.30
0.20
0.10
0.00
97
48
0
0.00 0.10 0.20 0.30 0.40 0.50 0.60
X distance (mm)

An important exception to the differential incorporation trend described above was noted by Reeder (1996) and Temmam et al. (2000), who showed that Zn(II) is preferentially incorporated in the $<\bar{4}41>_+$ steps, whereas enrichment in the $<\bar{4}41>_-$ steps would have been expected on the basis of its ionic radius, which is smaller than Ca. No satisfactory explanation was offered for this apparently anomalous behavior. A previous study used extended X-ray absorption fine structure (EXAFS) spectroscopy to confirm that Zn incorporated into calcite during growth occupies the Ca position in octahedral coordination, with Zn-O distances only slightly larger than in pure $ZnCO_3$ (Reeder et al., 1999).

A fundamental step in the overall sequence of trace element incorporation into a crystal structure is the initial attachment to surface sites (i.e., adsorption), and it has been suggested that Zn^{2+} may show a particular interaction with surface sites of calcite that leads to the observed preferential incorporation into the $<\bar{4}41>_+$ steps (Reeder, 1996). To address this possibility, we performed adsorption studies of Zn^{2+} on preequilibrated calcite and used EXAFS to characterize the adsorption complexes in situ. Our results suggest that the adsorption complex geometry almost certainly influences incorporation preferences. Additionally, the results characterize a potentially important retention mechanism of Zn in soils and sediments containing carbonate minerals, and complement earlier studies that have addressed Zn^{2+} adsorption to calcite.

Zachara et al. (1988, 1991) performed metal/calcite batch sorption studies for a series of divalent metals (Cd, Zn, Mn, Co, Ni, Ba, Sr) as a function of pH. At low initial metal concentrations ($<10^{-5}$ M), where metal retention was controlled by adsorption reactions rather than precipitation of metal carbonate and hydroxide phases, the data could be successfully described with a model assuming Me^{2+}-Ca^{2+} exchange at cation specific surface sites. For the divalent cations with ionic radii smaller than Ca^{2+}, the log-transformed exchange constants optimized in the fitting procedure increased linearly with ionic radius for Ni, Co, Mn, and Cd. Zinc, however, was anomalous with respect to this size trend, showing higher affinity for the calcite surface than expected on the basis of its ionic radius. On the basis of these findings, Zachara et al. (1991) suggested that factors other than ionic size, for instance the electronic environment of the metallic cation, also influenced the adsorption behavior.

More recently, Cheng et al. (1998) reported results from ex situ X-ray standing wave (XSW) and surface extended X-ray absorption fine structure (SEXAFS) spectroscopic studies of Zn^{2+} incorporated at the calcite $(10\bar{1}4)$ surface following interaction with Zn^{2+}-containing solutions. Zinc(II) was found to substitute for Ca^{2+} in the surface layer, accompanied by structural relaxation of the coordinating CO_3 ligands in response to the smaller size of Zn^{2+} as compared with the Ca^{2+} host. The SEXAFS results indicated a Zn-O radial distance very similar to the Zn-O bond length in pure $ZnCO_3$, which was also found by Reeder et al. (1999) for Zn incorporated into calcite during crystal growth.

Copper(II) is also an important species for which there have been few studies. Unlike the case of Zn, which forms the calcite isomorph $ZnCO_3$, $CuCO_3$ is not known to exist with the calcite structure, possibly as a result of the tendency for Cu^{2+} ($3d^9$) to undergo a Jahn-Teller distortion from octahedral coordination. Such distortion could also affect its adsorption behavior, as well as its incorporation into the calcite structure during coprecipitation. Previous studies have shown that calcium carbonates have a high affinity for Cu^{2+}, and that sorption proceeds rapidly, implying that calcium carbonates may be an important sink for Cu retention in natural systems (Franklin and Morse, 1982; Compton and Pritchard, 1990). Schosseler et al. (1999) examined Cu^{2+} uptake and speciation as a function of time in calcite and vaterite suspensions by in situ electron paramagnetic resonance (EPR) spectroscopy. In the vaterite suspensions, Cu^{2+} was found to change from a square planar or square pyramidal adsorbed surface species into an octahedral Jahn-Teller distorted bulk species as the vaterite transformed into calcite over time, forming a dilute $Cu_xCa_{(1-x)}CO_3$ solid solution. The same change in Cu^{2+} coordination was observed in the calcite suspensions, which had not been equilibrated with atmospheric CO_2 before reaction with Cu^{2+}, but at a slower rate when compared with the vaterite system. Here, we examine Cu^{2+} incorporation preferences between the nonequivalent steps on the calcite $(10\bar{1}4)$ surface. We also conduct Cu^{2+} adsorption experiments on calcite, and use EXAFS to characterize the Cu^{2+} adsorption complexes at the calcite surface, as well as the coordination of Cu^{2+} incorporated into calcite. As for Zn(II), our results suggest that the geometry of the Cu(II) adsorption complex at the calcite surface plays an important role in determining the preference of Cu(II) for incorporation into the structurally dissimilar steps on the $(10\bar{1}4)$ calcite surface.

2. MATERIALS AND METHODS

2.1. Adsorption Experiments

The calcite sorbent used in the adsorption experiments had an average particle size of 1.8 μm and a N_2-BET surface area of $\cong$10 m^2 g^{-1}. Before reaction with Cu^{2+} or Zn^{2+}, calcite-water suspensions containing 0.1 or 0.5 g calcite L^{-1} were equilibrated at atmospheric CO_2 pressure (i.e., in air) for 2 months. The suspension pH was measured at regular intervals during this period, and was found to stabilize at a value of 8.3 after $\sim$2 weeks. The equilibrated suspensions were spiked with Cu^{2+} or Zn^{2+} concentrations of 1.0, 5.0, or 10.0 μM by adding appropriate aliquots of 0.01 mol/L $CuCl_2$ or $ZnCl_2$ stock solutions. The suspension pH dropped by less than 0.05 pH unit when the metal was introduced, and was readjusted to the initial value within 2 min after metal addition with 0.1 M NaOH. The maximum loadings

Fig. 1. (a–c) DIC images of as-grown $(10\bar{1}4)$ surfaces of (a) Co^{2+}-doped, (b) Zn^{2+}-doped, and (c) Cu^{2+}-doped calcite crystals. The c-glide is vertical, with the c-axis 45° to the image pointing to the upper right. Polygonal shading patterns reveal two pairs of vicinal surfaces, labeled "+" and "−," which represent regions on the surface having growth steps oriented in different directions. Growth steps in the + vicinals, parallel to $[\bar{4}41]$ and $[48\bar{1}]$, are symmetrically equivalent, but are not equivalent to those in the − vicinals. Individual growth steps are not resolved. (d–f) Synchrotron μ-XRF maps corresponding to crystals in DIC images (a–c). Raw counts are plotted, and light shading indicates highest counts. Corresponding Ca maps are featureless. Cobalt(II) is preferentially incorporated at steps in the − vicinals, whereas Zn(II) and Cu(II) are preferentially incorporated at steps in the + vicinals.

(in case of 100% metal adsorption) for these samples were ~600 and 1200 mg metal kg^{-1} calcite (ppm). The samples were equilibrated for 2 d, and then filtered through 0.22 μm filter paper to collect the calcite solids for EXAFS analysis. Filtration was stopped while the calcite was still moist. The wet pastes were quickly loaded into lucite sample holders and sealed with Kapton tape to prevent drying. EXAFS spectra were collected immediately following filtration, and the samples were checked after data collection to confirm that they were still moist.

Speciation calculations performed with the chemical speciation program PHREEQC indicated that for Zn, the suspensions spiked with [Zn] = 5.0 μM and 10.0 μM were initially oversaturated with respect to hydrozincite ($Zn_5(OH)_6(CO_3)_2$) (but undersaturated with respect to smithsonite, $ZnCO_3$), having saturation index (SI) values of 0.56 and 2.06, respectively. The suspension spiked with [Zn] = 1.0 μM, however, was undersaturated with respect to any metal carbonate or hydroxide precipitate species, including hydrozincite. The solubility constant of hydrozincite provided by Schindler et al. (1969), and the Zn hydrolysis constants and solubility data of ZnO(s) reported by Bénézeth et al. (1999) were used in these calculations. For Cu(II), the suspension spiked with 5.0 μM was initially oversaturated with respect to malachite ($Cu_2(OH)_2CO_3$) (SI = 0.23), whereas the 1.0 μM suspension was undersaturated with respect to this solid. Comparison of the calcite samples reacted at the different levels of metal addition (particularly the EXAFS data of the 1.0 μM vs. the 5.0 μM and 10.0 μM samples) was used to evaluate the importance of precipitation reactions in the metal/calcite suspensions. Additionally, EXAFS spectra of hemimorphite ($Zn_4Si_2O_7(OH)_2.H_2O$), malachite ($Cu_2(OH)_2CO_3$), zincite (ZnO), and copper hydroxide ($Cu(OH)_2$) were collected and compared with those of the Cu/calcite and Zn/calcite sorption samples. The phase identity and purity of the standards was confirmed with XRD analyses.

2.2. Coprecipitation Experiments

The modified free-drift method described in detail by Paquette and Reeder (1995) and Reeder (1996) was used to synthesize Cu^{2+}-doped calcite crystals. Growth occurs at room temperature in a sealed reaction vessel with headspace in contact with a reservoir of solid ammonium carbonate. Steady-state decomposition of the ammonium carbonate produces NH_3(g) and CO_2(g), which dissolve into a $CaCl_2$-NH_4Cl growth solution, simultaneously increasing pH and carbonate alkalinity. Solution pH initially increases until calcite crystals begin nucleating on immersed glass substrates and vessel walls. The pH remains nearly constant (7.7 to 7.9) for as long as one week as calcite crystals increase in size, driven by the near steady-state supply of ammonium carbonate. Aqueous $CuCl_2$ was added after solution pH stabilized (following calcite nucleation). Despite the nearly constant pH during the coprecipitation period, the initial Ca^{2+} concentration (10 mM) decreased over the duration of the experiment (by up to 40%), and hence the solution composition was not strictly constant. Initial Cu^{2+} concentrations were in the range 50 to 200 μM for different experiments. Total CO_2 was determined in separate experiments via the procedure described by Hall and Aller (1992). This coprecipitation method requires a high ionic strength (~1.75 mol/L); NH_4Cl is used as a background electrolyte. Estimated SIs were in the range 0.6 to 0.8.

Water-clear calcite single crystals up to 700 μm were recovered from substrates and vessel walls, washed repeatedly in deionized water, and dried in air at 50 °C. Examination of the crystals showed them to be nearly perfect rhombohedra, exhibiting the common growth form $\{10\bar{1}4\}$. The growth surfaces appear macroscopically flat under reflected light, but differential interference contrast (DIC) microscopy reveals polygonized growth spirals (Fig. 1). Hence, growth occurred by the spiral mechanism, wherein attachment occurs primarily at kink sites within steps, which sweep around a dislocation growth center. Final Cu concentrations were determined by spatially resolved X-ray fluorescence (see below), yielding average concentrations in the 30 to 200 ppm range. Portions of the single crystal batches were ground to a fine powder for bulk XAS spectroscopy, loaded into aluminum holders, and sealed with Kapton tape. Other crystal were selected for micro–X-ray fluorescence (μ-XRF) work. For comparison, a natural calcite containing higher levels of incorporated Cu than the synthetically doped calcites was also analyzed by EXAFS.

Zn-doped calcite samples were taken from a previous study (Reeder et al., 1999). These synthetic samples were grown by following the same technique described above.

2.3. EXAFS Data Collection and Analysis

EXAFS spectra were recorded on beamlines X-11A and X-18B of the National Synchroton Light Source (NSLS) at Brookhaven National Laboratory. The storage ring operated at 2.84 GeV with a maximum current of 280 mA. A Si(111) crystal pair (X-11A) or a channel-cut Si(111) crystal (X-18B) was used in the monochromator, with detuning of 40% for harmonic rejection. The monochromator was calibrated with appropriate metal foils. Multiple scans of the Cu/calcite and Zn/calcite adsorption samples, as well as the dilute Cu- and Zn-calcite solid solutions prepared in the coprecipitation experiments, were collected at the Cu or Zn K-edge, with a 13-element Ge solid-state detector for fluorescence detection. The adsorption samples were run at room temperature, whereas the Zn- and Cu-doped calcite samples were run at liquid nitrogen temperature (77 K). The EXAFS data of the Cu and Zn solid standards were collected in transmission mode at room temperature or at liquid nitrogen temperature. Scans were calibrated and averaged before fitting. Further data reduction and fitting were performed with the WinXAS2000 software package using standard procedures (Ressler, 1997).

Theoretical backscattering paths were calculated with FEFF7 (Zabinsky et al., 1995) on the basis of input files of Cu(II) or Zn(II) substituting in the Ca site in calcite. Fitting was done in R space out to approximately 4 Å. For the adsorption samples, no constraints were placed on the fitting parameters of the first-neighbor O shells, but the Debye-Waller factors (σ^2) of the higher shells were fixed at 0.01 $Å^2$ to reduce the number of free parameters in the fitting procedure. The EXAFS data of the Zn- and Cu-doped calcite samples indicated that Cu and Zn occupied the Ca site in the calcite structure. To reduce the number of free parameters in the fitting procedure of these samples, the coordination numbers of the shells surrounding Cu and Zn atoms incorporated in calcite were therefore fixed at values consistent with Cu and Zn substitution in Ca sites, whereas all other parameters were allowed to vary. The number of parameters allowed to vary never exceeded the Nyguist limit. Error estimates are $\pm$0.02 Å for the R values of the first shells, and $\pm$0.05 Å for higher shells. For CN, which is correlated to the Debye-Waller factor, the error is estimated at $\pm$15% for the first O shell and >25% for the further shells.

2.4. μ-XRF

The Cu-doped growth experiments yielded calcite single crystals dominated by $(10\bar{1}4)$, corresponding to the common cleavage. Differential interference contrast microscopy revealed that individual $(10\bar{1}4)$ faces exhibited one or more growth hillocks (Fig. 1).

Crystals having a single well defined hillock were selected for mapping Cu distribution. The as-grown surface of a single crystal was mounted on a glass slide with a removable adhesive, ground, and polished to approximately 30 μm thickness, and finally remounted on a high-purity silica glass disk with the as-grown surface containing the growth hillock exposed. This permitted positioning of the X-ray beam on different vicinal faces of the growth hillock.

μ-XRF analysis was conducted at beamline X-26A at NSLS. Monochromatic radiation (~9.01 keV) was obtained by a channel-cut Si(111) monochromator, and the beam was focused with Kirkpatrick-Baez mirrors to produce a spot size of approximately 12 $\times$ 15 μm on the sample. The single crystal section was positioned at 45° to the incident beam, and an Si(Li) solid-state detector was used to collect characteristic fluorescence at 90°. Area scans were collected by rastering the sample relative to the beam position.

3. RESULTS

3.1. μ-XRF

Figure 1 presents the results of X-ray fluorescence microanalyses of calcite $(10\bar{1}4)$ hillocks grown in coprecipitation experiments with divalent Cu, Zn, and Co. The Co and Zn results have been reported previously by Reeder (1996) and are

shown here for comparison with the Cu-doped crystals. Figure 1 shows that divalent Cu, Zn, and Co, despite similar ionic radii (for sixfold coordination: 0.745, 0.73, and 0.74 Å, for Co, Cu, and Zn, respectively; Shannon, 1976), exhibit different preferences for incorporation among multiple surface sites present on the calcite ($10\bar{1}4$) face during spiral growth. Cobalt(II) is preferentially incorporated into the parallel arrays of $<\bar{4}41>_-$ steps that define one pair of symmetrically equivalent vicinal faces on polygonized growth spirals. In contrast, Cu(II) and Zn(II) are preferentially incorporated into $<\bar{4}41>_+$ growth steps, which define the second pair of vicinal faces on the growth spirals but are symmetrically nonequivalent to the steps on the first pair.

As discussed in the introduction, previous work has shown that the ion size of the substituting divalent metal cation relative to the Ca host plays an important role in the preference of metal for incorporation into the $<\bar{4}41>_+$ steps. Divalent metal ions smaller than Ca tend to be preferentially incorporated in the $<\bar{4}41>_-$ steps, whereas substituting metals larger than Ca are preferentially incorporated into the $<\bar{4}41>_+$ steps (Paquette and Reeder, 1995; Reeder, 1996). In Reeder (1996) and Temmam et al. (2000) it was noted, however, that Zn(II), which has an ionic radius smaller than Ca(II), showed anomalous behavior with respect to this size trend because it is preferentially incorporated in $<\bar{4}41>_+$ steps. The results presented here demonstrate that Cu(II) is also preferentially taken up in the $<\bar{4}41>_+$ steps despite its smaller ionic radius relative to the Ca(II) host. The EXAFS results discussed below suggest that the interaction between the substituting metal and calcite surface sites in the adsorption step plays an important role in metal site preference during calcite crystal growth, and may explain the observed preference of Cu(II) and Zn(II) for the $<\bar{4}41>_+$ steps.

3.2. EXAFS Data

3.2.1. Adsorption samples

Figure 2a, b show the raw and fitted k^3-weighted χ spectra of the Zn/calcite and Cu/calcite adsorption samples, and shown in Figure 2c, d are the radial structure functions (RSF) obtained by Fourier transforming the raw x spectra. Also shown are the EXAFS data of the various Cu(II) and Zn(II) solid standards. For both Cu^{2+} and Zn^{2+}, the EXAFS data of the metal/calcite adsorption samples reacted at metal concentrations of 1.0 μM (undersaturated with respect to malachite and hydrozincite, respectively) are essentially identical to those of the calcite suspensions spiked with metal concentrations of 5.0 μM and 10.0 μM. This suggests that no significant precipitation has occurred in the metal/calcite suspensions with Cu(II) or Zn(II) concentrations of 5.0 μM and 10.0 μM, despite the initial oversaturation with respect to hydrozincite and malachite in these samples for Zn(II) and Cu(II), respectively. Indeed, in the case of Cu^{2+}, the EXAFS spectrum of malachite is very different from the Cu/calcite adsorption spectra (Fig. 2), indicating that this precipitate had not formed to any noticeable extent in the sorption samples. For Zn^{2+}, the EXAFS fitting results of the adsorption samples are inconsistent with hydrozincite precipitation, as will be discussed below. We therefore conclude that the calcite sorbent adsorbed sufficient Cu^{2+} and Zn^{2+} to prevent precipitation of malachite and hydrozincite under the reaction conditions studied here, and that the Cu/calcite and Zn/calcite sorption EXAFS data shown in Figure 2 represent adsorbed metal species at the calcite surface. For Zn^{2+}, this conclusion is consistent with the findings of Zachara et al. (1988, 1989), who reported that Zn^{2+} retention in calcite suspensions is controlled by adsorption reactions below (initial) Zn^{2+} concentrations of $\sim 10^{-5}$ M and by hydrozincite precipitation at Zn^{2+} concentrations $>10^{-5}$ M in adsorption experiments with very similar surface area to metal ratios as employed in our study.

The fitted equatorial Cu-O distance for malachite ($R_{Cu\text{-}O}$ = 1.93 Å; Table 1) is shorter than the average equatorial Cu-O distance on the basis of the crystal structure of this Cu compound ($R_{Cu\text{-}O}$ = 1.985 Å; Suesse, 1967). Copper(II) in malachite occupies two different sites, both of which have significantly distorted equatorial O shells, with distances ranging between 1.900 and 2.116 Å. The relatively short $R_{Cu\text{-}O}$ distance found in the EXAFS analysis of the equatorial O shell indicates that scattering from this shell is disproportionally dominated by the close O atoms.

The fitting results obtained for the Cu/calcite and Zn/calcite adsorption samples indicated that scattering from oxygen atoms located at a radial distance of $\sim$1.95 Å from the central metal absorber dominated the spectra in both cases (Table 1). Peaks at longer radial distances in the RSF (Figs. 2b, d) indicate scattering from O, C, and Ca located in shells beyond the first O ligand shell, consistent with the formation of inner-sphere Cu^{2+} and Zn^{2+} sorption complexes at the calcite surface, where Cu and Zn atoms are linked to Ca metal centers via carbonate ligands. Such direct chemical bonding between the calcite surface and Cu^{2+} and Zn^{2+} is notable, as inner-sphere metal adsorption complexes are expected to be less susceptible to desorption than electrostatically held outer-sphere complexes. Calcite may therefore play an important role in immobilizing these trace metals in natural systems via adsorption reactions.

Zinc(II) is usually found in 4- or sixfold coordination with first-shell O ligands. The Zn-O bond length can be used to distinguish between these Zn-O coordination geometries: Zn-O distances of $\sim$1.96 Å are typical of tetrahedral coordination, whereas Zn-O distances of $\sim$2.10 Å indicate octahedral coordination (e.g., Shannon, 1976). This is illustrated by the first-shell Zn-O distances found for the Zn reference compounds. In both ZnO and hemimorphite, Zn(II) is tetrahedrally coordinated by O, and the Zn-O distances found in our EXAFS analyses are 1.96 Å and 1.94 Å, respectively (Table 1). This agrees within error with the Zn-O distances of 1.978 and 1.955 Å derived from XRD analyses of these compounds (Hill et al., 1977; Albertsson et al., 1989). In contrast, $ZnCO_3$ contains Zn in octahedral coordination with first-neighbor O, and the EXAFS analyses yield a Zn-O distance of 2.10 Å for this compound, which again agrees within error with XRD data ($R_{Zn\text{-}O}$ = 2.111 Å; Effenberger et al., 1981). On the basis of the first-shell Zn-O distances of 1.95 Å found for the Zn/calcite adsorption samples (Table 1), we therefore conclude that the Zn adsorption complexes at the calcite surface are predominantly tetrahedrally coordinated by O, although the possibility of the presence of a small fraction of octahedral complexes can not be excluded. We further note that the Zn-O distances observed for the Zn

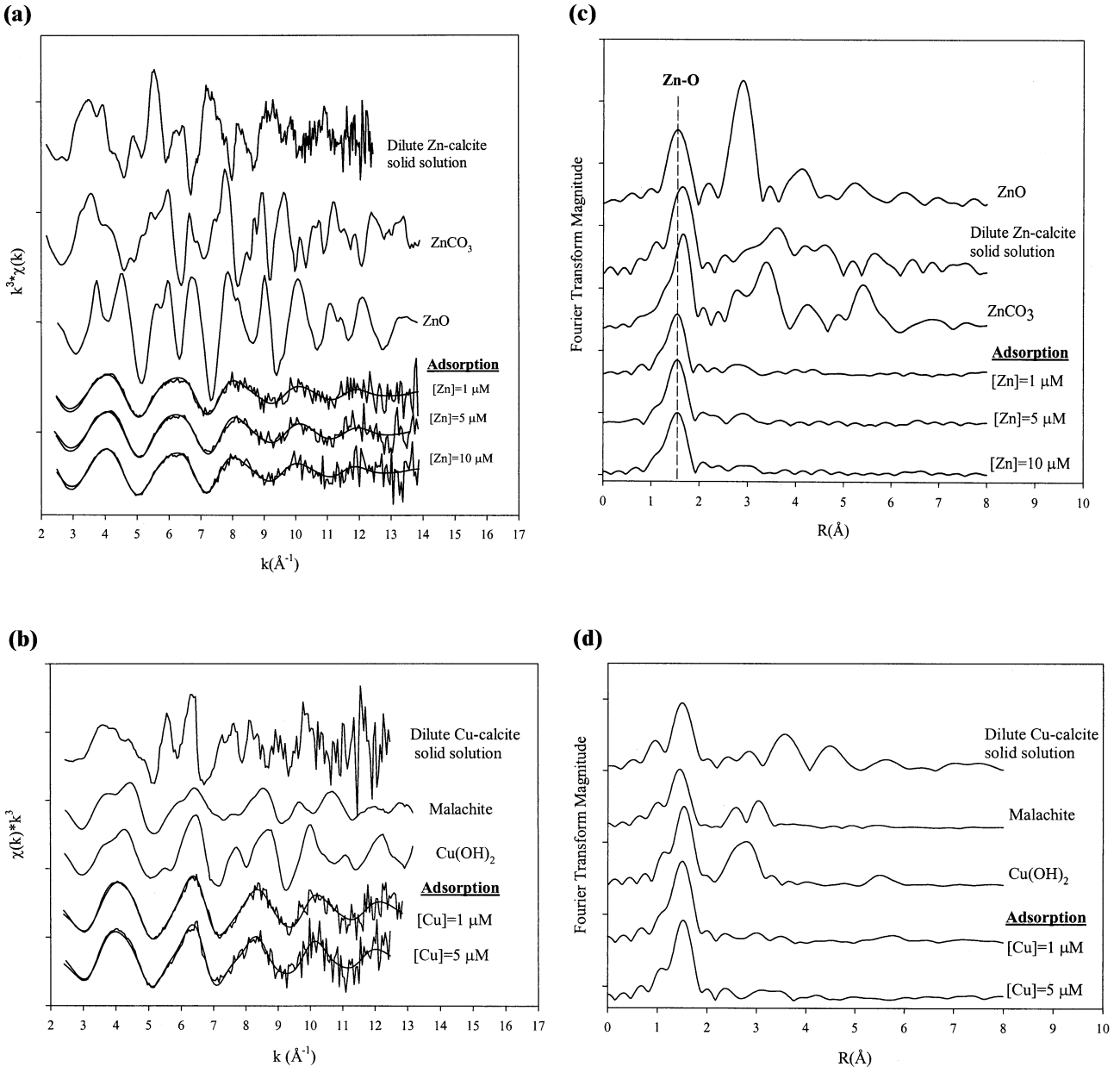

Fig. 2. (a, b) The k^3-weighted $\chi(k)$ of the Zn(II) and Cu(II) adsorption samples and reference compounds, and (c, d) the corresponding Fourier transforms (not corrected for phase shift) of these spectra. Fits are shown for the adsorption samples in k space.

adsorption samples are inconsistent with hydrozincite precipitation. Hydrozincite ($Zn_5(OH)_6(CO_3)_2$) contains three different Zn sites, two of which are octahedral with average $R_{Zn\text{-}O}$ = 2.10 and 2.11 Å, and one tetrahedral with average $R_{Zn\text{-}O}$ = 1.95 Å (Ghose, 1964). The relative abundance of these sites is 1:2:2, yielding a (weighted) average Zn-O distance of 2.05 Å. The results of hydrozincite EXAFS analyses reported by Charnock et al. (1996) are in good agreement with these values. The average Zn-O distance of hydrozincite is significantly longer than the Zn-O distances observed for the Zn/calcite adsorption samples, confirming that hydrozincite precipitation had not occurred to any significant extent in the adsorption experiments.

In addition to the observed Zn-O distance of 1.95 Å, the tetrahedral coordination of the Zn/calcite adsorption complexes is also supported by the near-edge spectra in Figure 3, which shows the normalized white line of the Zn/calcite adsorption sample reacted at [Zn] = 1.0 μM along with those of hemimorphite, zincite, $ZnCO_3$ and $Zn_xCa_{1-x}CO_3$ samples. Rose et al. (2001) noted that the normalized intensity of the Zn K-edge white line is suppressed for compounds with tetrahedral Zn-O coordination as compared with octahedral Zn-O coordination, as a result of the difference in 4p character of the associated electronic transitions. As shown in Figure 3, the normalized white line of the Zn/calcite adsorption sample is distinctively less intense than those of the $ZnCO_3$ and $Zn_xCa_{1-x}CO_3$ com-

Table 1. Structural parameters derived from EXAFS analysis of the adsorption and reference samples.

	Sorption samples				Reference samples[a]				
Sample	Shell	N	R(Å)	σ^2(Å^2)	Compound	Shell	N	R(Å)	σ^2(Å^2)
1 μM Zn	Zn-O	4.4	1.95	0.008	ZnO	Zn-O	4.3	1.96	0.005
	Zn-C	3.7	2.86	0.01[b]			*4*	*1.981*	
	Zn-O	2.3	3.05	0.01[b]		Zn-Zn	10.9	3.21	0.009
	Zn-Ca	1.3	3.33	0.01[b]			*6*	*3.199*	
							6	*3.242*	
5 μM Zn	Zn-O	4.3	1.95	0.007					
	Zn-C	4.1	2.87	0.01[b]	Hemimorphite[c]	Zn-O	3.4	1.94	0.003
	Zn-O	3.4	3.07	0.01[b]			*4*	*1.956*	
	Zn-Ca	1	3.35	0.01[b]					
					$ZnCO_3$	Zn-O	6.7	2.09	0.006
10 μM Zn (short Ca fit)	Zn-O	4.7	1.96	0.009			*6*	*2.111*	
	Zn-C	3.4	2.86	0.01[b]		Zn-C	6[b]	2.99	0.008
	Zn-O	1.4	3.04	0.01[b]			*6*	*2.964*	
	Zn-Ca	1.1	3.35	0.01[b]		Zn-O	6[b]	3.22	0.003
							6	*3.231*	
10 μM Zn (long Ca fit)	Zn-O	4.5	1.96	0.008		Zn-Zn	6[b]	3.66	0.005
	Zn-C	1.8	2.83	0.01[b]			*6*	*3.673*	
	Zn-O	2.3	3.23	0.01[b]					
	Zn-Ca	1.1	3.85	0.01[b]	$Cu(OH)_2$	Cu-O	3.6	1.95	0.005
							4	*1.96*	
						Cu-Cu	2.1	2.95	0.008
1 μM Cu	Cu-O	4.4	1.94	0.006			*2*	*2.95*	
	Cu-C	2.6	2.95	0.01[b]		Cu-Cu	3.8	3.25	0.013
	Cu-O	1.2	3.30	0.01[b]			*4*	*3.34*	
	Cu-Ca	1.2	3.89	0.01[b]					
					Malachite[c]	Cu-O	3.4	1.93	0.008
5 μM Cu	Cu-O	4.1	1.96	0.005			*4*	*1.985*	
	Cu-C	2.6	2.95	0.01[b]					
	Cu-O	1.5	3.35	0.01[b]					
	Cu-Ca	1.8	3.90	0.01[b]					
$Zn_xCa_{(1-x)}CO_3$	Zn-O	7.1	2.13	0.008					
	Zn-C	6[b]	3.13	0.005					
	Zn-O	6[b]	3.36	0.006					
	Zn-Ca	6[b]	3.95	0.005					
$Cu_xCa_{(1-x)}CO_3$	Cu-O	4.1	2.01	0.006					
	Cu-C	6[b]	2.99	0.007					
	Cu-O	6[b]	3.21	0.015					
	Cu-Ca	6[b]	3.97	0.007					
Calcite[a]	Ca-O	*6*	*2.360*						
	Ca-C	*6*	*3.213*						
	Ca-O	*6*	*3.459*						
	Ca-Ca	*6*	*4.048*						

[a] Italics indicate structural parameters derived from XRD crystallographic data.
[b] Fixed values.
[c] Only O shell was fitted.

pounds, which have Zn in octahedral coordination, whereas it is similar in intensity to the zincite and hemimorphite white lines, which have Zn in tetrahedral coordination.

The electronic configuration of Cu(II) causes it to undergo a Jahn-Teller distortion from octahedral geometry, with four equatorial O ligands close to the Cu metal center, and one or two axial O atoms at longer radial distances. The Cu/calcite adsorption EXAFS spectra are dominated by first shell O atoms located at a Cu-O radial distance of ~1.95 Å, which are the equatorial oxygens of the Jahn-Teller distorted Cu atoms at the calcite surface. Similar Cu-O distances for the equatorial O shell of Cu atoms sorbed at mineral surfaces have been reported in other studies (Weesner and Bleam, 1997; Schosseler et al., 1999; Cheah et al., 2000; Alcacio et al., 2001; Morton et al., 2001). In the $Cu(OH)_2$ reference sample, the equatorial O shell is found at 1.95 Å, in good agreement with XRD results (Oswald et al., 1990).

The RSFs presented in Figure 2 show scattering from atoms located beyond the (dominant) first O shell in the EXAFS data of the Cu/calcite and Zn/calcite adsorption samples. Fitting these longer correlations required O, C, and Ca shells, which indicates that Cu and Zn are coordinated to CO_3 ligands at the calcite surface. For Cu, best fits were obtained with O, C, and Ca shells located at ~2.95, 3.30 and 3.90 Å, respectively (Fig. 2b and Table 1). These values are consistent with Cu positioned in unoccupied Ca sites at the calcite surface. This configuration

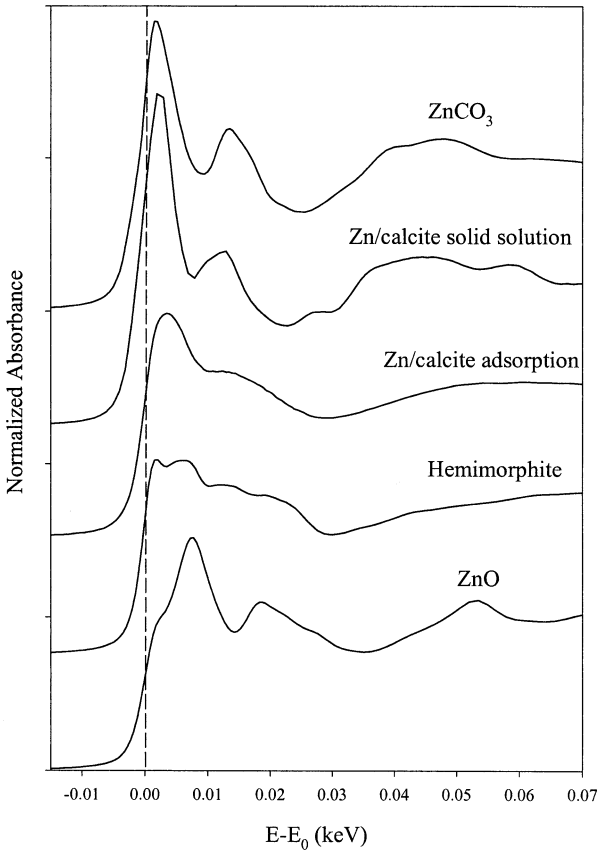

Fig. 3. Normalized near-edge spectra of [Zn] = 1.0 μM adsorption sample compared with spectra of tetrahedral (hemimorphite and zincite) and octahedral ($ZnCO_3$ and $Zn_xCa_{1-x}CO_3$) Zn compounds. The intensity of the white line is markedly suppressed in the Zn/calcite adsorption sample and the tetrahedral reference samples relative to the octahedrally coordinated Zn compounds.

would require one of the axial oxygens to be involved in the surface coordination. Although it was possible to fit a small axial O contribution at approximately 2.6 Å, this did not improve the fit, and resulted in a high Debye-Waller factor for this shell, which indicates high structural and/or thermal disorder in the Cu-O_{axial} correlation. This suggests that the axial water ligands may not have been replaced by O-CO_2 surface ligands via a ligand exchange process in the adsorption step, but possibly are weakly bonded to surface carbonate groups via hydrogen bonding.

For the Zn/calcite adsorption samples, good fits were obtained with C and O shells located at ~2.86 and 3.05 Å, respectively, and a Ca shell at approximately 3.35 Å (Fig. 2a and Table 1). These fits were generated on the basis of the assumption that the peak at ~3.0 Å visible in the RSF (uncorrected for phase shift) of the adsorption samples shown in Figure 2c represents Ca atoms in the coordination sphere of sorbed Zn. It was possible, however, to obtain fits of similar quality with C and O shells located at ~2.8 and 3.2 Å, and a Ca shell at 3.85 Å (Table 1), as illustrated in Figure 4 for the [Zn] = 10 μM adsorption sample. The first Zn-O shell parameters (particularly the Zn-O radial distance) in this fit did not change relative to those of the fit with close Ca shells (Table 1).

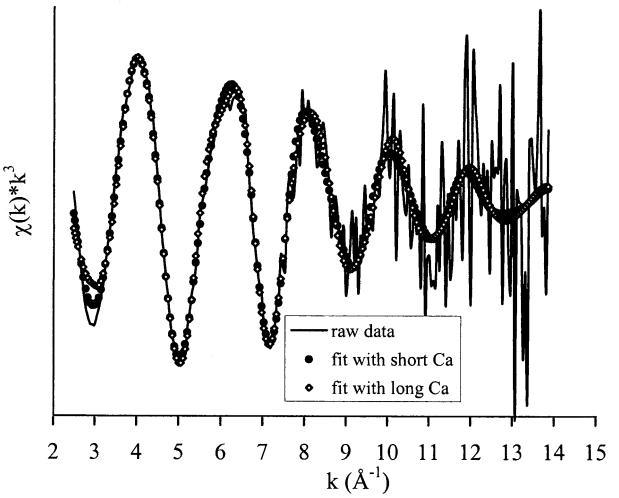

Fig. 4. Comparison between raw χ data and fits assuming short (3.35 Å) or long (3.85 Å) Zn-Ca correlations for the adsorption sample reacted at [Zn] = 10 μM. Both sets of fitting parameters are presented in Table 1.

Because of (1) the weak backscattering from shells located beyond the dominant first-neighbor O shell, (2) the presence of three (partly overlapping) shells in the second coordination sphere of sorbed Zn, and (3) the deterioration of the EXAFS signal beyond ~9 $Å^{-1}$ in these dilute samples, no definitive choice between these fitting results can be made on the basis of the EXAFS data. Calculating Zn-Ca distances for Zn tetrahedrons positioned in surface Ca sites indicated that both Zn-Ca distances can be achieved by changing the degree of relaxation of the coordinating surface CO_3 groups. Because the degree of structural relaxation of the surface carbonates is not known, we can not state a preference for either of the fits shown in Table 1 and Figure 4. Both sets of fitting results are, however, consistent with Zn tetrahedrons adsorbed at kinks and steps on the corners, faces and edges of crystals, which contain Ca and CO_3 that are only partially coordinated by lattice atoms and are thus expected to be the most reactive toward Zn (and Cu) complexation.

3.2.2. Dilute calcite solid solutions

Figure 5 shows the fits in R space (both the magnitude and imaginary parts of the Fourier transformed k^3-weighted χ spectra) of natural and synthetic Cu- and Zn-doped calcites; the fitting results for these samples are reported in Table 1. For Cu, the natural sample is shown because we were not able to collect good quality EXAFS data of synthetic Cu-doped calcite. As shown in the inset of Figure 5a, however, the near-edge structure of the synthetic Cu-doped sample is very similar to that of the natural sample, indicating a similar coordination of Cu in both cases. The EXAFS fitting results for these samples (Table 1) are consistent with Cu and Zn occupying Ca sites in the calcite structure, indicating the formation of dilute metal-calcite solid solutions. The smaller ion size of Cu and Zn as compared with Ca distorts the local coordination around the incorporated metal ions, which is reflected in Me-O, Me-C, and Me-Ca distances shorter than those found in the ideal calcite structure.

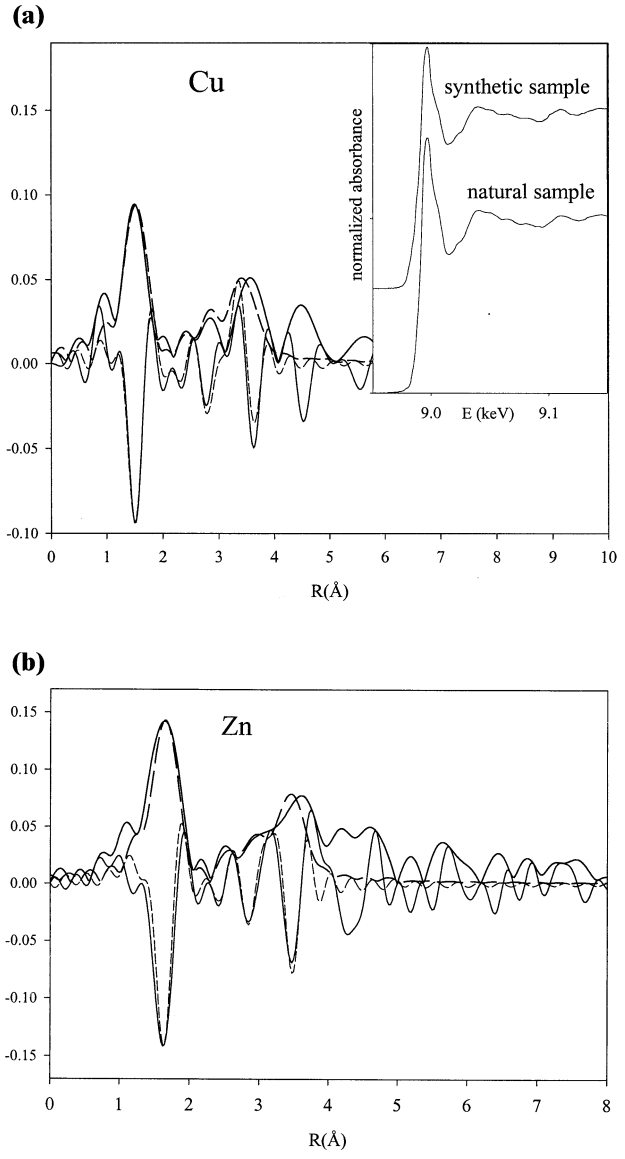

Fig. 5. Magnitude and imaginary components of R-space fits for (a) natural Cu-doped and (b) synthetic Zn-doped calcite. Raw data are presented as solid lines; fits are presented as dashed lines. The inset in (a) compares the near-edge XAS spectra of synthetic and natural Cu-doped calcites.

This is consistent with the results reported by Reeder et al. (1999).

Incorporated Zn atoms are octahedrally coordinated by O with a Zn-O distance of 2.13 Å, which is slightly longer than the Zn-O distance of 2.10 Å optimized for $ZnCO_3$ (Table 1). This slight dilation of the Zn-O distance in dilute solid solution relative to that in pure $ZnCO_3$ is a relaxation effect also observed for Co substitution in calcite (Reeder et al., 1999). EXAFS analyses of the dilute Cu-calcite solid solution indicates that Cu atoms are substituting for Ca in the calcite structure as Jahn-Teller distorted octahedra, with the four equatorial oxygens located at 2.01 Å. This equatorial radial distance is consistent with the results of Schosseler et al. (1999), who reported a bond length of 2.0 Å for the equatorial shell surrounding Cu incorporated in calcite on the basis of EPR characterization of dilute Cu-calcite solid solutions. The axial bond length in the study of Schosseler et al. (1999) was estimated at 2.3 Å. As for the sorption samples, we were not able to reliably fit an axial O contribution for the incorporated Cu atoms.

Our results indicate that the oxygen coordinations observed for the Cu and Zn adsorption complexes at the calcite surface are different from those of Zn and Cu incorporated in the calcite structure, especially in the case of Zn. The difference in Me-O coordination between adsorbed and bulk Cu and Zn species indicates that the transformation of Cu and Zn surface complexes into incorporated species involves a substantial rearrangement of the first neighbor O shell. This is particularly true for Zn, which transforms from a tetrahedral adsorption complex into an octahedrally coordinated Ca substitute in calcite during crystal growth.

Cheng et al. (1998) used XSW triangulation and surface SEXAFS spectroscopy to characterize the molecular configuration of Zn(II) at the calcite ($10\bar{1}4$) surface following reaction with Zn(II)-containing solution. A Zn-O radial distance of 2.11 Å was found for the four in-plane coordination O atoms, and the radial distance of the out of plane O atoms was estimated at 1.95 Å. These results indicate incorporation of Zn in the calcite surface lattice as octahedral complexes during reaction of the calcite ($10\bar{1}4$) surface with the Zn-containing solution. This is markedly different from our results, which indicate that the Zn/calcite adsorption complexes are tetrahedral with $R_{Zn\text{-}O}$ = 1.95 Å. In the Cheng et al. (1998) study, the calcite was reacted with Zn-EDTA solutions that were undersaturated with respect to calcite, whereas our studies were done in calcite saturated solutions without EDTA. Moreover, the spectroscopic measurements of Cheng et al. (1998) were done ex situ, following removal of solution from the calcite surface with a jet of N_2 gas, whereas our EXAFS spectra were collected on wet samples. It is likely that these differences in experimental setup explain the differences between our results and those of Cheng et al. (1998).

4. DISCUSSION

4.1. Adsorption Complexes

Figure 6 presents possible configurations of the Zn(II) and Cu(II) adsorption complexes forming at kinks and steps at the calcite surface, on the basis of the EXAFS results of the Zn/calcite and Cu/calcite adsorption samples presented above. Coordination to three carbonate functional groups is considered here because this is expected to be the minimum number of complexing carbonates required to anchor an adsorbing metal ion in a surface Ca site. The O-O distance between the nearest oxygens of neighboring CO_3 groups in the calcite structure is 3.26 Å for carbonate groups within the same carbonate layer, and 3.41 Å for carbonate groups located in adjacent layers (Reeder, 1983; Paquette and Reeder, 1995). The O-O separation in the first-neighbor O shell of the Cu and Zn adsorption complexes is 2.76 Å and 3.19 Å, respectively, as calculated based on the first shell Me-O distances found in the EXAFS analyses and the idealized (i.e., nondistorted) geometries of the adsorption complexes. The discrepancy between the carbonate and metal O-O separations implies that substantial displacements from the calcite CO_3 position are required to accommo-

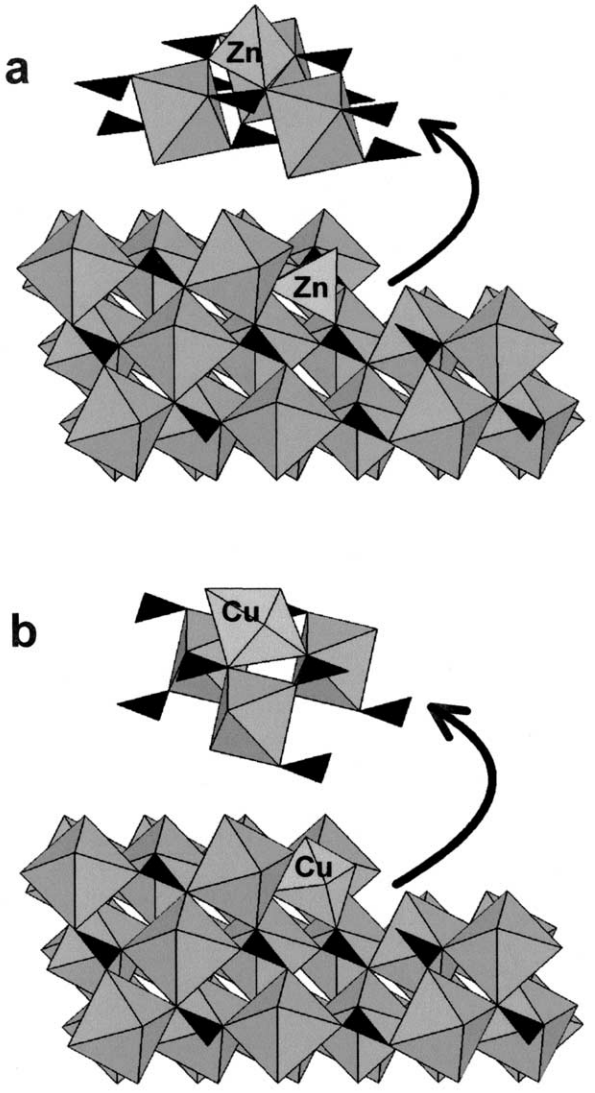

Fig. 6. Possible configurations of the Zn(II) and Cu(II) adsorption complexes forming at kinks and steps at the calcite surface, based on the EXAFS results of the Zn/calcite and Cu/calcite adsorption samples.

date the metal complexes at the surface, especially in the case of Cu(II). Carbonate groups in the calcite structure act as rigid units, that may, however, twist to coordinate to foreign metal ions of different size than the Ca host, as has been demonstrated in studies of Co, Zn, Pb, and Ba incorporation in the calcite crystal structure (Reeder et al., 1999). At the surface, where the carbonate groups are not fully coordinated by Ca, their flexibility to bind such metal ions is expected to be even greater than in the bulk. Results of X-ray reflectivity studies presented by Fenter et al. (2000) suggested that CO_3 groups on the terrace portions of the $(10\bar{1}4)$ face are in fact slightly rotated relative to their position in the bulk.

4.2. Implications for Differential Me(II) Incorporation at the Calcite $(10\bar{1}4)$ Surface

The molecular characteristics of the Zn^{2+} and Cu^{2+} adsorption complexes, particularly the first-shell Me-O coordination, may explain the preferred uptake of these trace metals in the $<\bar{4}41>_+$ steps, which have structurally different surface sites than the $<\bar{4}41>_-$ steps. The $<\bar{4}41>_+$ steps contain sites with three equal O-O distances of 3.26 Å, whereas the surface sites in the $<\bar{4}41>_-$ steps have two O-O distances of 3.41 Å and one O-O distance of 3.26 Å (Paquette and Reeder, 1995). Fitting the Zn and Cu adsorption complexes, which have short O-O distances, into Ca sites in the $<\bar{4}41>_+$ steps requires less distortion of the calcite CO_3 positions than placing them in sites in the $<\bar{4}41>_-$ steps, which may partially explain the favored uptake of these metals in the $<\bar{4}41>_+$ steps. Such structural considerations, however, cannot fully account for the incorporation preference of Cu and Zn for the $<\bar{4}41>_+$ steps. Octahedral Co(II) in $CoCO_3$(s) for instance, has basal edge O-O distances of 2.947 Å, and diagonal edge O-O distances of 3.019 Å, which, from a structural point of view, would better match with the $<\bar{4}41>_+$ steps than with the $<\bar{4}41>_-$ steps; yet, Co(II) is preferentially incorporated into the $<\bar{4}41>_-$ steps (Reeder, 1996). Unlike Zn^{2+} and Cu^{2+}, Co^{2+} is expected to adsorb as a regular octahedron, on the basis of the results of EXAFS studies of Co(II) adsorption complexes forming at mineral surfaces (O'Day et al., 1994; Thompson et al., 1999; Towle et al., 1999). It would seem, therefore, that the distortion from regular octahedral geometry observed for the Zn and Cu adsorption complexes plays an important role in their preference for the $<\bar{4}41>_+$ steps. Possibly, the larger 'mismatch' of the O-O distances of the sites in the $<\bar{4}41>_-$ steps for incorporation of divalent metal ions as compared with those in the $<\bar{4}41>_+$ steps is compensated by energetic considerations, which may make coordination in the $<\bar{4}41>_-$ steps more favorable than uptake at $<\bar{4}41>_+$ steps in the case of octahedral adsorption complexes. This energy gain may be offset by the entropy gain of Zn adsorbing as an tetrahedral complex, and the energy gain of the Jahn-Teller distortion of the Cu adsorption complex. This, then, possibly places more importance on structural considerations (i.e., the "match" between surface site geometry and metal adsorption complex geometry), resulting in preferred uptake of Cu and Zn in the $<\bar{4}41>_+$ steps.

On the basis of the results of the Cu and Zn adsorption studies and coprecipitation experiments and the arguments outlined below, we propose that for the divalent metals considered here (i.e., Cu, Zn, Co, Cd, Mg, Mn, Sr, Ba, Pb), the key factor determining preference for incorporation at specific surface sites on the calcite $(10\bar{1}4)$ plane is the geometry of the adsorption complex, with octahedral adsorption complexes preferentially incorporating in the $<\bar{4}41>_-$ steps, and nonoctahedral complexes in the $<\bar{4}41>_+$ steps. Although spectroscopic characterization of the adsorption complexes formed by these metals at the calcite surface is very limited, and further studies are needed to characterize these complexes, results from spectroscopic studies that use other substrates (clay minerals and metal oxides) than calcite are consistent with our hypothesis. The other divalent metals besides Cu^{2+} and Zn^{2+} that have been shown to incorporate preferentially in the $<\bar{4}41>_+$ steps are Ba^{2+}, Sr^{2+}, and Pb^{2+}. These metals rarely exist as octahedral complexes, mainly as a result of their large size:charge ratio, as well as the presence of a lone pair of electrons in the case of Pb^{2+}. Spectroscopic studies of the adsorption complexes these metals form at the calcite surface have been reported only for Sr^{2+}. On the basis of EXAFS results, Parkman et al. (1998)

reported that the adsorption complexes of Sr^{2+} forming at the calcite mineral surface remained partially hydrated, resulting in (nonoctahedral) Sr adsorption complexes with first-shell Sr-O coordination numbers higher than 6. Similarly, Sahai et al. (2000) concluded on the basis of EXAFS data that the adsorption complexes of Sr^{2+} on goethite, amorphous silica and kaolinite remain hydrated and have (nonoctahedral) coordinations similar to that of Sr^{2+} (aq). No spectroscopic studies have been reported on Pb adsorption to calcite; however, EXAFS studies of Pb^{2+} adsorption to iron-, manganese-, and aluminum-oxides have shown that the Pb^{2+} inner-sphere complexes formed at these surfaces have distorted trigonal pyramidal oxygen configurations (Bargar et al., 1997a,b; Matocha et al., 2001). Because Ba(II) is even larger than Sr(II), it is unlikely that Ba(II) adopts an octahedral O geometry upon adsorption to mineral surfaces. Although further study is needed to confirm the nonoctahedral geometry of Pb and Ba adsorption complexes on calcite, the studies indicated above show that these metals tend to be nonoctahedral when adsorbed at mineral surfaces. EXAFS studies of Cu and Zn adsorption complexes on Fe- and Al-oxides have shown Jahn-Teller distorted Cu complexes and tetrahedral Zn adsorption complexes on these surfaces, similar to our observations on calcite (Trainor et al., 2000; Alcacio et al., 2001; Waychunas et al., 2002).

For the divalent metals that are enriched in the $<\bar{4}41>_-$ steps (Mg, Cd, Co, Mn), no spectroscopic studies exist on the coordination of their adsorption complexes at the calcite surface. However, results of EXAFS studies that use Fe- and Al-oxides and clay minerals as substrates have shown exclusively octahedral O coordination for Cd (Spadini et al., 1994; Collins et al., 1999; Parkman et al., 1999) and Co (O'Day et al., 1994; Thompson et al., 1999; Towle et al., 1999) when adsorbed to these mineral surfaces, so most likely, these metals also form octahedral adsorption complexes at the calcite surface. For the divalent metals considered here, we therefore propose that the key factor determining preference for incorporation at specific surface sites on the calcite $(10\bar{1}4)$ plane is the geometry of the adsorption complex, with octahedral adsorption complexes preferentially incorporating in the $<\bar{4}41>_-$ steps, and nonoctahedral complexes in the $<\bar{4}41>_+$ steps.

5. CONCLUSIONS

X-ray fluorescence microanalyses of calcite $(10\bar{1}4)$ hillocks grown in coprecipitation experiments show that divalent Cu and Zn, which have ionic radii smaller than Ca, are preferentially incorporated into the parallel arrays of $<\bar{4}41>_+$ steps that define one pair of symmetrically equivalent vicinal faces on polygonized growth spirals. In contrast, other divalent metals with sixfold ionic radii smaller than Ca (e.g., Co, Cd, Mn, Mg) are preferentially incorporated into $<\bar{4}41>_-$ growth steps, which define the second pair of vicinal faces on the growth spirals but are symmetrically nonequivalent to the steps on the first pair. EXAFS results of dilute Cu- and Zn-calcite solid solutions are consistent with Cu and Zn substitution in the Ca site of calcite. To address the possibility that a particular interaction between Zn and Cu and the calcite surface leads to the observed preference of these metals for the $<\bar{4}41>_+$ steps, we performed EXAFS studies of Cu(II) and Zn(II) adsorption complexes at the calcite surface. The results indicate that both Cu(II) and Zn(II) reside at Ca sites on the calcite surface, likely at kinks and steps, forming mononuclear inner-sphere adsorption complexes. For adsorbed Zn(II), a tetrahedral coordination with respect to first-neighbor O ligands is found, whereas Cu(II) forms Jahn-Teller distorted adsorption complexes. The distortion from octahedral symmetry observed for the Cu and Zn adsorption complexes is proposed to play a key role in the preference of Cu and Zn for incorporation into the $<\bar{4}41>_+$ steps. The observed formation of inner-sphere Cu(II) and Zn(II) adsorption complexes at the calcite surface implies that carbonate minerals may play an important role in retaining these trace metals in calcareous soils and sediments via adsorption reactions.

Acknowledgments—Funding for this work was provided by DOE grant DE-FG07-99ER15013 through the Environmental Management Science Program and by NSF grant EAR9706012. We thank A. Lanzirotti (X26A, NSLS), S. Khalid, W. Caliebe (X18B, NSLS), and K. Pandya (X11A, NSLS) for assistance with data collection. Comments from N. Sturchio and two anonymous reviewers improved the final manuscript.

Associate editor: S. J. Traina

REFERENCES

Albertsson J., Abrahams S. C., and Kvick A. (1989) Atomic displacements, anharmonic thermal vibration, expansivity and pyroelectric coefficient thermal dependences in ZnO. *Acta Crystallogr.* **B45,** 34–40.

Alcacio T. E., Hesterberg D., Chou J. W., Martin J. D., Beauchemin S., and Sayers D. E. (2001) Molecular scale characteristics of Cu(II) bonding in goethite–humate complexes. *Geochim Cosmochim. Acta* **65,** 1355–1366.

Bargar J. R., Brown G. E. Jr., and Parks G. A. (1997a) Surface complexation of Pb(II) at oxide–water interfaces. I. XAFS and bond-valence determination of mononuclear and polynuclear Pb(II) sorption products on aluminum oxides. *Geochim. Cosmochim. Acta* **61,** 2617–2637.

Bargar J. R., Brown G. E. Jr., and Parks G. A. (1997b) Surface complexation of Pb(II) at oxide–water interfaces. II. XAFS and bond-valence determination of mononuclear Pb(II) sorption products and surface functional groups on iron oxides. *Geochim. Cosmochim. Acta* **61,** 2639–2652.

Bénézeth P., Palmer D. A., and Wesolowski D. J. (1999) The solubility of zinc oxide in 0.03 m NaTr as a function of temperature, with in situ pH measurement. *Geochim Cosmochim. Acta* **63,** 1571–1586.

Charnock J. M., Schofield P. F., Henderson C. M. B., Cressey G., and Cressey B. A. (1996) Cu and Zn ordering in aurichalcite. *Mineral. Mag.* **60,** 887–896.

Cheah S. F., Brown G. E. Jr., and Parks G. A. (2000) XAFS study of Cu model compounds and Cu^{2+} sorption products on amorphous SiO_2, g-Al_2O_3, and anatase. *Am. Mineral.* **85,** 118–132.

Cheng L., Sturchio N. C., Woicik J. C., Kemner K. M., Lyman P. F., and Bedzyk M. J. (1998) High-resolution structural study of zinc ion incorporation at the calcite cleavage surface. *Surf. Sci.* **415,** L976–L982.

Collins C. R., Ragnarsdottir K. V., and Sherman D. M. (1999) Effect of inorganic and organic ligands on the mechanism of cadmium sorption to goethite. *Geochim Cosmochim. Acta* **63,** 2989–3002.

Compton R. G. and Pritchard K. L. (1990) Kinetics of Langmuirian adsorption of Cu(II) ions at calcite/water interface. *J. Chem. Soc. Faraday Trans.* **86,** 129–136.

Davis K. J., Dove P. M., and De Yoreo J. J. (2000) The role of Mg^{2+} as an impurity in calcite growth. *Science* **290,** 1134–1137.

Effenberger H., Mereiter K., and Zemann J. (1981) Crystal structure refinements of magnesite, calcite, rhodochrosite, siderite, smithsonite, and dolomite, with discussion of some aspects of the stereochemistry of calcite type carbonates. *Z. Kristallogr.* **156,** 233–243.

Fenter P., Geissbuhler P., DiMasi E., Srajer G., Sorensen L. B., and Sturchio N. C. (2000) Surface speciation of calcite observed in situ by high-resolution X-ray reflectivity. *Geochim Cosmochim. Acta* **64,** 1221–1228.

Franklin M. L. and Morse J. W. (1982) The interaction of copper with the surface of calcite. *Ocean Sci. Eng.* **7,** 147–174.

Ghose S. (1964) The crystal structure of hydrozincite, $Zn_5(OH)_6(CO_3)_2$. *Acta Crystallogr.* **17,** 1051–1057.

Gratz A. J., Hillner P. E., and Hansma P. K. (1993) Step dynamics and spiral growth on calcite. *Geochim. Cosmochim. Acta* **57,** 491–495.

Hall P. O. and Aller R. C. (1992) Rapid, small-volume flow-injection analysis for ΣCO_2 and NH_4^+ in marine and fresh waters. *Limnol. Oceanogr.* **37,** 1113–1119.

Hill R. J., Gibbs G. V., Craig J. R., Ross F. K., and Williams J. M. (1977) A neutron-diffraction study of hemimorphite. *Z. Krist.* **146**, 241–259.

Lorens R. B. (1981) Sr, Cd, Mn, and Co distribution coefficients in calcite as a function of calcite precipitation rate. *Geochim. Cosmochim. Acta* **45,** 553–561.

Matocha C. J., Elzinga E. J., and Sparks D. L. (2001) Reactivity of Pb(II) at the Mn(III,IV) (oxyhydr)oxide–water interface. *Env. Sci. Technol.* **35,** 2967–2972.

Morse J. W. and Bender M. L. (1990) Partition coefficients in calcite: Examination of factors influencing the validity of experimental results and their application to natural systems. *Chem. Geol.* **82,** 265–277.

Morton J. D., Semrau J. D., and Hayes K. F. (2001) An X-ray aborption spectroscopy study of the structure and reversibility of copper adsorbed to montmorillonite clay. *Geochim. Cosmochim. Acta* **65,** 2709–2722.

Mucci A. and Morse J. W. (1990) Chemistry of low-temperature abiotic calcites: Experimental studies on coprecipitation, stability and fractionation. *Aquat. Sci.* **3,** 217–254.

O'Day P. A., Brown G. E. Jr., and Parks G. A. (1994) Molecular structure and binding sites of cobalt(II) surface complexes on kaolinite from X-ray absorption spectroscopy. *Clays Clay Minerals* **42,** 337–355.

Oswald H. R., Reller A., Schmalle H. W., and Dubler E. (1990) Structure of copper $^{2+}$ hydroxide, $Cu(OH)_2$. *Acta Crystallogr.* **C46,** 2279–2284.

Parkman R. H., Charnock J. M., Livens F. R., and Vaughan D. J. (1998) A study of the interaction of strontium ions in aqueous solution with the surfaces of calcite and kaolinite. *Geochim. Cosmochim. Acta* **62,** 1481–1492.

Parkman R. H., Charnock J. M., Bryan N. D., Livens F. R., and Vaughan D. J. (1999) Reactions of copper and cadmium ions in aqueous solutions with goethite, lepidocrocite, mackinawite, and pyrite. *Am. Mineral.* **84,** 407–419.

Paquette J. and Reeder R. J. (1990) New type of compositional zoning in calcite: Insights into crystal growth mechanisms. *Geology* **18,** 1244–1247.

Paquette J. and Reeder R. J. (1995) Relationship between surface structure, growth mechanism, and trace element incorporation in calcite. *Geochim. Cosmochim. Acta* **59,** 735–749.

Reeder R. J. (1983) Crystal chemistry of the rhombohedral carbonates. In *Carbonates: mineralogy and chemistry* (ed. R. J. Reeder). Reviews in Mineralogy Volume 11, pp 1–47.

Reeder R. J. (1996) Interaction of divalent cobalt, zinc, cadmium, and barium with the calcite surface during layer growth. *Geochim. Cosmochim. Acta* **60,** 1543–1552.

Reeder R. J., Lamble G. M., and Northrup P. A. (1999) XAFS study of the coordination and local relaxation around Co^{2+}, Zn^{2+}, Pb^{2+}, and Ba^{2+} trace elements in calcite. *Am. Mineral.* **84,** 1049–1060.

Ressler T. (1997) WinXAS: A new software package not only for the analysis of energy-dispersive XAS data. *J. Physique IV* **7,** C2–269.

Rimstidt J. D., Balog A., and Webb J. (1998) Distribution of trace elements between carbonate minerals and aqueous solutions. *Geochim. Cosmochim. Acta* **62,** 1851–1863.

Rose J., Moulin I., Masion A., and Bertsch P. M. (2001) X-ray absorption spectroscopy study of immobilization processes for heavy metals in calcium silicate hydrates. 2. Zinc. *Langmuir* **17,** 3658–3665.

Sahai N., Carroll S. A., Roberts S., and O'Day P. A. (2000) X-ray absorption spectroscopy of strontium(II) coordination—II. Sorption and precipitation at kaolinite, amorphous silica, and goethite surfaces. *J. Colloid Interface Sci.* **223,** 198–212.

Schindler P., Reinert M., and Gamsjäger H. (1969) Löfslichkeitskonstanten und frei Bildungsenthalpien von $ZnCO_3$ und $Zn_5(OH)_6(CO_3)_2$ bei 25°C. *Helv. Chim. Acta* **52,** 2327–2332.

Schosseler P. M., Wehrli B., and Schweiger A. (1999) Uptake of Cu^{2+} by the calcium carbonates vaterite and calcite as studied by continuous wave (CW) and pulse electron paramagnetic resonance. *Geochim. Cosmochim. Acta* **63,** 1955–1967.

Shannon R. D. (1976) Revised effective ionic radii and systematic studies of interatomic distances in halides and chalcogenides. *Acta Crystallogr.* **A32,** 751–767.

Spadini L., Manceau A., Schindler P. W., and Charlet L. (1994) Structure and reversibility of Cd^{2+} surface complexes on ferric oxides. 1. Results from EXAFS spectroscopy. *J. Colloid Interface Sci.* **168,** 73–86.

Suesse P. (1967) Verfeinerung der Kristallstruktur des Malachits, $Cu_2(OH)_2CO_3$. *Acta Crystallogr.* **22,** 146–151.

Temmam M., Paquette J., and Vali H. (2000) Mn and Zn incorporation into calcite as a function of chloride aqueous concentration. *Geochim. Cosmochim. Acta* **64,** 2417–2430.

Teng H. H., Dove P. M., and DeYoreo J. J. (1999) Reversed calcite morphologies indicated by microscopic growth kinetics: Insight into biomineralization. *Geochim. Cosmochim. Acta* **63,** 2507–2512.

Thompson H. A., Parks G. A., and Brown G. E. Jr. (1999) Dynamic interactions of dissolution, surface adsorption, and precipitation in an aging cobalt(II)-clay–water system. *Geochim. Cosmochim. Acta* **63,** 1767–1779.

Towle S. N., Bargar J. R., Brown G. E. Jr., and Parks G. A. (1999) Sorption of Co(II) on metal oxide surfaces II. Identification of Co(II)(aq) adsorption sites on the (0001) and $(1\bar{1}02)$ surfaces of α-Al_2O_3 by grazing-incidence XAFS spectroscopy. *J. Colloid Interface Sci.* **217,** 312–321.

Trainor T. P., Brown G. E. Jr., and Parks G. A. (2000) Adsorption and precipitation of aqueous Zn(II) on alumina powders. *J. Colloid Interface Sci.* **231,** 359–372.

Waychunas G. A., Fuller C. C., and Davis J. A. (2002) Surface complexation and precipitate geometry for aqueous Zn(II) sorption on ferrihydrite I: X-ray absorption extended fine structure spectroscopy analysis. *Geochim. Cosmochim. Acta* **66,** 1119–1137.

Weesner F. J. and Bleam W. F. (1997) X-ray absorption and EPR spectroscopic characterization of adsorbed copper(II) complexes at the boehmite (AlOOH) surface. *J. Colloid Interface Sci.* **196,** 79–86.

Zabinsky S. I., Rehr J. J., Ankudinov A., Albers R. C., and Eller M. J. (1995) Multiple-scattering calculations of X-ray absorption spectra. *Phys. Rev.* **B52,** 2995–3009.

Zachara J. M., Kittrick J. A., and Harsh J. B. (1988) The mechanism of Zn^{2+} adsorption on calcite. *Geochim Cosmochim. Acta* **52,** 2281–2291.

Zachara J. M., Kittrick J. A., Dake L. S., and Harsh J. B. (1989) Solubility and surface spectroscopy of zinc precipitates on calcite. *Geochim Cosmochim. Acta* **53,** 9–19.

Zachara J. M., Cowan C. E., and Resch C. T. (1991) Sorption of divalent metals on calcite. *Geochim. Cosmochim. Acta* **55,** 1549–1562.